DNS STUDY OF TURBULENT HEAT TRANSFER IN A CIRCULAR PIPE SUBJECTED TO AXIAL SYSTEM ROTATION

Zhao-Ping Zhang and Bing-Chen Wang
Department of Mechanical Engineering
University of Manitoba
Winnipeg, MB, R3T 5V6, Canada
BingChen.Wang@umanitoba.ca

ABSTRACT

Turbulent heat transfer in a pipe flow subjected to axial system rotation is studied using direct numerical simulation (DNS) for a wide range of rotation numbers varying from $Ro_b = 0$ to 20. At moderate and high rotation numbers, the axial system rotation tends to reduce the mean temperature, temperature variance and axial turbulent heat flux, while increase the Nusselt number and suppress the turbulent scalar energy (TSE) level of the flow. Two types of flow structures are involved in the heat convection process. The first type is hairpin structures of the turbulent boundary layer developing over the pipe wall. The second type is the Taylor columns only appearing at relative high rotation numbers. Owing to the axial system rotation, the pressure diffusion-redistribution and Coriolis production terms dominate the transport of turbulent heat fluxes. As the rotation number increases, the streaky thermal structures become increasingly elongated in the near-wall region of the pipe, resulting in heat transfer enhancement at high rotation numbers.

INTRODUCTION

Turbulent heat transfer in an axially-rotating pipe flow is a challenging problem which is frequently encountered in engineering applications such as rotating heat exchangers and rotary machines. In an axially-rotating circular pipe flow, Coriolis forces arise which further induce large secondary flow motions in the cross-stream direction. The energetic secondary flows influence considerably not only the flow statistics and coherent structures but also the performance of turbulent heat transfer.

Compared with the study of turbulent heat transfer through a stationary (non-rotating) circular pipe flow, the number of experimental and numerical investigations of turbulent heat convection in an axially-rotating pipe flow is rather limited in the literature. Cannon & Kays (1969) conducted the first experiment to investigate the effects of axial rotation on turbulent heat transfer in a circular pipe flow. They observed that the system rotation suppressed turbulent velocity fluctuations in the near-wall region of the pipe. As the rotation number increased, the turbulent flow became increasingly laminarized as the convective heat transfer rate decreased. Reich & Beer (1989) measured turbulent heat and fluid flow in an axially-rotating pipe flow using laser Doppler velocimetry (LDV). They observed that the friction factor and Nusselt number reduced considerably with an increasing rotation number. Satake & Kunugi (2002) performed direct numerical simulation (DNS) to study a heated axially-rotating pipe flow under a uniform peripheral wall heat flux condition. In their research, the effects of axial system rotation were investigated through various turbulence statistics of the velocity and temperature fields. Ould-Rousis *et al.* (2010) compared DNS and large-eddy simulation (LES) results of the turbulent heat transfer in an axially-rotating pipe flow under identical thermal boundary conditions. They observed that the axial and azimuthal turbulent heat fluxes significantly reduced and augmented, respectively, as the rotation number increased. By contrast, the axial system rotation had only a slight influence on the radial component of turbulent heat flux. Bousbai *et al.* (2013) conducted LES to investigate the effects of axial system rotation on the turbulent heat convection in a pipe flow. They observed that the degree of intermittency as indicated by the skewness and flatness factors of the temperature fluctuations tended to increase near the pipe wall as the rotation number increased.

Based on a thorough literature review, it is noticed that detailed DNS studies of turbulent heat convection in an axially-rotating turbulent pipe flow are still rather scarce, and in-depth understanding of the effects of Coriolis forces on the temperature statistics and thermal structures needs to be developed. In view of this knowledge gap, we aim to conduct a systematic DNS study of turbulent heat transfer in a circular pipe subjected to axial system rotation for a wide range of rotation numbers, which is the first objective of this research.

Furthermore, among a few available DNS studies of axially-rotating pipe flows in the literature, the longest pipe was that used in Orlandi & Ebstein (2000), which had a pipe length of $L_z = 25R$ (or, $7.96\pi R$), where R is the pipe radius. In order to reasonably capture the energetic axial eddy motions and precisely reproduce the physical process of heat convection, very long pipes are used in our DNS, which constitutes the second objective of this research. The range of pipe lengths of this research is $L_z = 30\pi R$-$180\pi R$, such that the shortest and longest pipes are 3.77 and 22.62 times of that used in the DNS of Orlandi & Ebstein (2000). Comparatively speaking, the long pipes used in our current DNS studies demand a significant increase of the computational efforts.

TEST CASE AND NUMERICAL ALGORITHM

Figure 1 shows the computational domain under axial system rotation at a counterclockwise angular speed Ω_z. The radial, azimuthal and axial coordinates of the cylindrical coordinate system are denoted using r, β and z, and the corresponding velocity components are denoted as u_r, u_β and u_z, respectively. Depending upon the rotation number, the pipe length varies from $L_z = 30\pi R$ (at $Ro_b = 0$) to $180\pi R$ (at $Ro_b = 20$) to ensure that energetic turbulent eddy motions are reasonably captured in the z-direction. The specific pipe lengths in regard to different rotation numbers are given in Tab. 1. The pipe flow is fully developed at Reynolds number of $Re_\tau = 180$ and Prandtl number of $Pr = 1$. In total, eight test cases of rotation

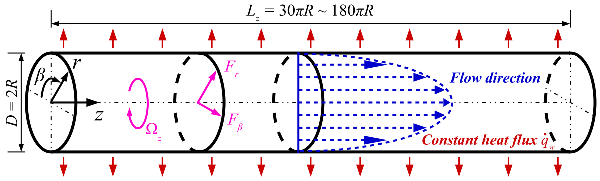

Figure 1. Schematic of the computational domain of an axially-rotating circular pipe in cylindrical coordinate system. F_r and F_β are two Coriolis force components in radial and azimuthal directions, respectively. The pipe flow is cooled along the axial direction by imposing a constant wall heat flux ($\dot{q}_w$) on the curved wall.

Table 1. Summary of eight rotating cases tested.

Case #	1	2	3	4	5	6	7	8
Ro_b	0	1	2	4	6	10	14	20
L_z	$30\pi R$	$30\pi R$	$30\pi R$	$60\pi R$	$60\pi R$	$90\pi R$	$120\pi R$	$180\pi R$
N_z	3600	3600	3600	5400	5400	6000	6400	7200
Δz^+	4.712	4.712	4.712	6.283	6.283	8.482	10.603	14.137

numbers ranging from $Ro_b = 0$ to 20 are compared. Periodic boundary condition and no-slip condition are applied to the z-direction and on the pipe surface, respectively. A uniform peripheral wall heat flux ($\dot{q}_w$) boundary condition is imposed on the pipe wall for cooling the flow. Here, $Ro_b = 2\Omega_z R/U_b$ and $Re_\tau = u_\tau R/\nu$, where U_b is the bulk mean velocity, u_τ is the wall friction velocity, and ν is the kinematic viscosity of the fluid. The governing equations for an incompressible flow with respect to an axial rotating reference frame are

$$\nabla \cdot \vec{u} = 0 \quad , \tag{1}$$

$$\frac{\partial \vec{u}}{\partial t} + \vec{u} \cdot \nabla \vec{u} = -\Pi \hat{\mathbf{e}}_z - \frac{1}{\rho} \nabla p + \nu \nabla^2 \vec{u} + \vec{F} \quad , \tag{2}$$

$$\frac{\partial \theta}{\partial t} + \vec{u} \cdot \nabla \theta = -u_z \frac{dT_w}{dz} + \alpha \nabla^2 \theta \quad , \tag{3}$$

where $\vec{u}$, ρ, α, p and θ are the velocity, density, thermal diffusivity, pressure and deficit temperature (defined as $\theta = T - T_w$) of the fluid, respectively. Π and dT_w/dz represent the constant mean axial pressure and temperature gradients, respectively. Specifically, $dT_w/dz = d\theta_b/dz = 2\dot{q}_w/(\rho C_p U_b R)$, where T_w is the local mean peripheral temperature at wall, θ_b is the bulk mean temperature, and C_p is the specific heat capacity of the fluid. As shown schematically in Fig. 1, in response to the axial rotation, two components of the Coriolis force $\vec{F}$ appear in the r- and β-directions, i.e., $F_r = -2\Omega_z u_\beta$ and $F_\beta = 2\Omega_z u_r$.

The DNS was performed with a spectral-element code so-called "Semtex" by Blackburn & Sherwin (2004). The quadrilateral spectral-element method was applied which divides the cross-section of the pipe into 420 finite elements, with each element further discretized spatially with 8th-order Gauss-Lobatto-Legendre Lagrange interpolants. As is shown in Tab. 1, depending upon the rotation number, the physical quantities were expanded into the spectral space using Fourier series with $N_z = 3600$-7200 modes in the z-direction. Therefore, the total grid points varied from $N_{tot} = 97$ to 194 million. The grid spacing in three directions are $\Delta z^+ = 4.712$-14.137, $\Delta r^+ = 0.123$-3.595, and $R\Delta\beta^+ = 0.813$-5.133, respectively. All simulations were held at a constant time step of $\Delta t^+ = u_\tau^2 \Delta t/\nu = 0.0122$. Here, the friction velocity is defined as $u_\tau = \sqrt{-\Pi R/2}$. For each tested case, 300 instantaneous snapshots over 40 large-eddy turnover times (LETOTs, defined as R/u_τ) with 1.4-2.8 TB data were generated on the supercomputers of the Digital Research Alliance of Canada.

In analogy with a turbulent boundary-layer flow over a flat plate, a dimensionless coordinate is applied for studying the thermal behavior of the flow in the circular pipe, i.e., $y \overset{\text{def}}{=} 1 - r/R$. Moreover, In order to non-dimensionalize the temperature statistics, the wall friction temperature needs to be introduced which is defined as $\theta_\tau = -\dot{q}_w/(\rho C_p u_\tau)$.

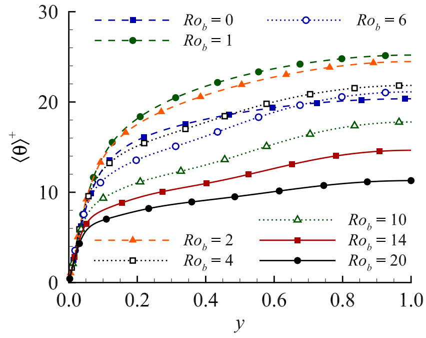

(a) Mean temperature $\langle\theta\rangle^+$

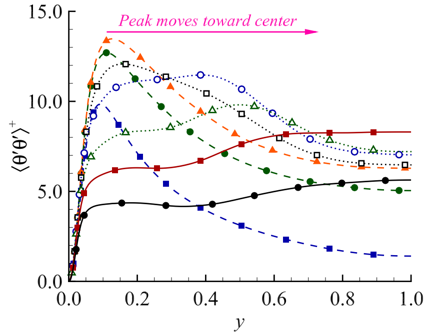

(b) Temperature variance $\langle\theta'\theta'\rangle^+$

Figure 2. Profiles of mean temperature $\langle\theta\rangle^+$ and temperature variance $\langle\theta'\theta'\rangle^+$ at eight different rotation numbers for $Ro_b = 0$-20. All values are non-dimensionalized by θ_τ.

RESULTS AND DISCUSSIONS

Figure 2 compares the profiles of the mean temperature $\langle\theta\rangle^+$ and temperature variance $\langle\theta'\theta'\rangle^+$ with respect to the wall normal distance y at eight different rotation numbers. Here, $\langle\cdot\rangle$ denote averaging over the time and over the homogeneous directions. Clearly, the profiles of $\langle\theta\rangle^+$ and $\langle\theta'\theta'\rangle^+$ are axial-symmetric, varying non-monotonically with Ro_b. As shown in Fig. 2(a), the peak value of $\langle\theta\rangle^+$ augments by 23.77% at the pipe center as the rotation number increases from $Ro_b = 0$ to 1. As Ro_b further increases to 20, the peak magnitude decreases considerably, which is 44.54% lower than that of $Ro_b = 0$. In Fig. 2(b), the profile of $\langle\theta'\theta'\rangle^+$ peaks at $y = 0.093$ for the non-rotating pipe flow. Owing to the system rotation imposed, the peak of $\langle\theta'\theta'\rangle^+$ increases at $y = 0.127$ at $Ro_b = 2$, and then reduces monotonically at the pipe center at $Ro_b = 20$. It is evident that the peak position tends to shift toward the pipe center when as the rotation number increases from $Ro_b = 0$ to 20. Meanwhile, the profile of $\langle\theta'\theta'\rangle^+$ turns into a single-peak pattern from a dual-peak pattern in the entire r-direction. Clearly, the system rotation behaves to suppress the TSE level in the near-wall region of the pipe.

Figure 3 shows the bulk mean temperature θ_b^+, volumed-averaged TSE k_θ^+ and Nusselt number Nu/Nu_{ref} as a function of rotation number Ro_b. Their definitions read as

$$\theta_b = \frac{2}{U_b R^2} \int_0^R \langle u_z \rangle \langle \theta \rangle r\, dr \quad , \tag{4}$$

$$k_\theta = \frac{2}{R^2} \int_0^R \langle \theta' \theta' \rangle r\, dr \quad , \tag{5}$$

$$Nu = \frac{hD}{K} = \frac{2R}{\theta_b} \frac{\partial \langle \theta \rangle}{\partial y} \bigg|_{y=0} \quad , \tag{6}$$

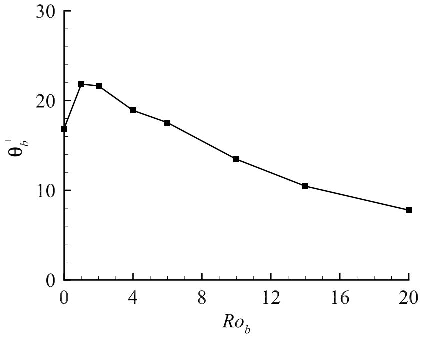

(a) Bulk mean temperature θ_b^+

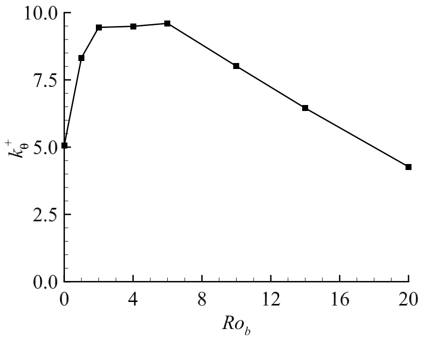

(b) Volume-averaged TSE k_θ^+

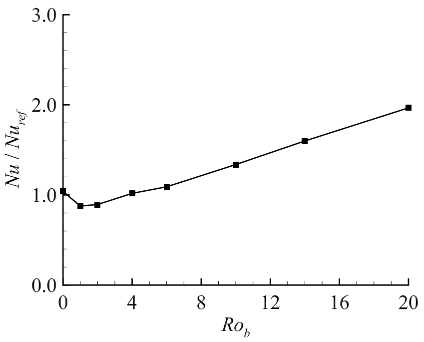

(c) Nusselt number Nu/Nu_{ref}

Figure 3. Profiles of bulk mean temperature θ_b^+, volume-averaged TSE k_θ^+ and Nusselt number Nu/Nu_{ref} with respect to rotation number Ro_b. In panels (a,b), the values of θ_b^+ and k_θ^+ have been non-dimensionalized by θ_τ. In panel (c), all values are further treated by dividing Nu_{ref} determined from the Gnielinski correlation.

respectively. Here, h is the convective heat transfer coefficient, and K is the thermal conductivity of the fluid. In Fig. 3(a), the profile of θ_b^+ peaks at $Ro_b = 1$, with a magnitude that is 29.38% higher than that of $Ro_b = 0$. As Ro_b increases beyond 1, the value of θ_b^+ reduces dramatically. From Fig. 3(b), it is seen that the profile of k_θ^+ increases considerably with Ro_b and reaches its maximum at $Ro_b = 6$. As Ro_b continues to increase to 20, the value of k_θ^+ decreases by 15.62% in comparison with that of $Ro_b = 0$. It is clear from Fig. 3(b) that the mechanism of the axial system rotation is to inject TSE into the pipe flow if $Ro_b \leq 6$. However, once Ro_b is higher than 6, the system rotation tends to suppress the TSE level. In Fig. 3(c), the Nusselt number Nu is further treated by dividing Nu_{ref} determined from the Gnielinski correlation. The minimum value of Nu is observed at $Ro_b = 1$, which is 15.5% lower than that of $Ro_b = 0$. When Ro_b increases beyond 1, the value of Nu enhances dramatically, and reaches its maximum at $Ro_b = 20$, with a magnitude that is 89.4% higher than that of $Ro_b = 0$. From Figs. 3(a-c), it is evident that the axial system rotation

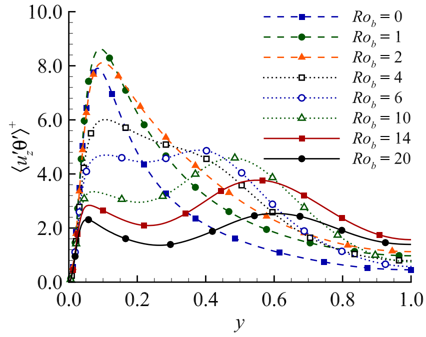

(a) Axial component $\langle u_z'\theta' \rangle^+$

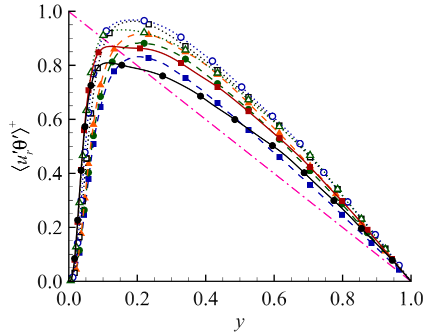

(b) Radial component $\langle u_r'\theta' \rangle^+$

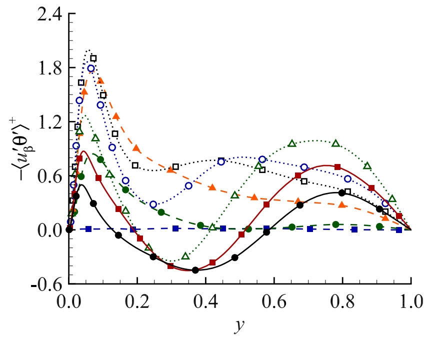

(c) Azimuthal component $\langle u_\beta'\theta' \rangle^+$

Figure 4. Profiles of turbulent heat fluxes $\langle u_z'\theta' \rangle^+$, $\langle u_r'\theta' \rangle^+$ and $\langle u_\beta'\theta' \rangle^+$ at eight different rotation numbers for $Ro_b = 0$-20. All values are non-dimensionalized by u_τ and θ_τ.

tends to promote the thermal energy transport at high rotation numbers.

Figure 4 compares the turbulent heat fluxes $\langle u_z'\theta' \rangle^+$, $\langle u_r'\theta' \rangle^+$, and $\langle u_\beta'\theta' \rangle^+$ at eight rotation numbers tested. All profiles are axial-symmetric about the pipe center ($y = 1.0$). In Fig. 4(a), the magnitude of $\langle u_z'\theta' \rangle^+$ varies non-monotonically in the near-wall region with Ro_b, and reaches its maximum at $y = 0.093$ at $Ro_b = 1$. As Ro_b further increases to 20, the system rotation tends to lessen the magnitude of $\langle u_z'\theta' \rangle^+$. Meanwhile, the profile of $\langle u_z'\theta' \rangle^+$ evolves from a dual-peak to a quadruple-peak pattern along a diameter. From Fig. 4(b), the profile of $\langle u_r'\theta' \rangle^+$ is strictly linear and symmetric about the pipe center at $Ro_b = 0$. However, as soon as the system rotation is imposed, the profile of $\langle u_r'\theta' \rangle^+$ deviates from this linear characteristic. The maximum value of $\langle u_r'\theta' \rangle^+$ is observed at $y = 0.187$ at $Ro_b = 6$. In Fig. 4(c), $\langle u_\beta'\theta' \rangle^+$ is trivial at $Ro_b = 0$, but its magnitude varies non-monotonically with Ro_b. At $Ro_b = 4$, the magnitude of $\langle u_\beta'\theta' \rangle^+$ reaches its maximum at $y = 0.058$. Moreover, the shape of $\langle u_r'\theta' \rangle^+$ remains stable and crosses zero five times over a diameter (in the entire r-direction) if $Ro_b \geq 10$.

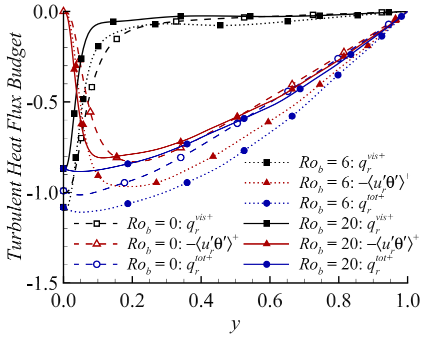

Figure 5. Budget profiles of radial heat flux q_r^+ at three rotation numbers $Ro_b = 0$, 6 and 20. q_r^{vis+} and $-\langle u_r'\theta'\rangle^+$ represent viscous and turbulent heat fluxes, respectively. All radial heat fluxes are non-dimensionalized by u_τ and θ_τ.

By applying turbulence decomposition (i.e., $\theta = \langle\theta\rangle + \theta'$) to the thermal energy equation (3), the following radial heat flux decomposition can be obtained

$$q_r^{tot+} = q_r^{vis+} - \langle u_r'\theta'\rangle^+ = \frac{2}{1-y}\int_y^1 \frac{\langle u_z\rangle}{U_b}(y-1)\,dy \quad , \quad (7)$$

where q_r^{tot} and q_r^{vis} represent total heat flux and viscous heat flux (expressed as $\alpha\partial\langle\theta\rangle/\partial r$) of the radial direction, respectively. Figure 7 shows the decomposition of the radial heat flux at three different rotation numbers $Ro_b = 0$, 6 and 20. Clearly, all three profiles of $-\langle u_r'\theta'\rangle^+$, q_r^{tot+} and q_r^{vis+} are sensitive to the rotation number, although the Coriolis force (as indicated by Ω_z) does not explicitly show in Eq. (7). The influence of the axial system rotation on the transport of thermal energy is through the convection of the fluid flow.

Figure 6 compares the premultiplied axial cross-spectrum of axial, radial and azimuthal velocity-temperature fluctuations $k_z^+\widetilde{Q}_z^+$, $k_z^+\widetilde{Q}_r^+$ and $k_z^+\widetilde{Q}_\beta^+$ calculated along the streamwise direction at wall-normal positions $y = 0.093$, 0.187 and 0.058, respectively. The 1D axial cross-spectrum is defined as

$$\widetilde{Q}_i(k_z) = \mathrm{Re}\left\{\overline{\widehat{u_i'}^*\,\widehat{\theta'}}\right\} \quad , \quad (8)$$

where an overbar represents temporal averaging, and operator Re$\{\cdot\}$ and superscript "*" denote the real part and conjugate of a complex number, respectively. A hat denotes Fourier transform in the axial direction of an arbitrary variable $\phi(r,\beta,k_z,t)$, i.e.

$$\hat{\phi}(r,\beta,k_z,t) = \frac{1}{L_z}\int_0^{L_z}\phi(r,\beta,z,t)e^{-\underline{\mathrm{i}}k_z z}dz \quad , \quad (9)$$

where $\underline{\mathrm{i}} = \sqrt{-1}$ is the imaginary unit and $k_z = n_z k_{0z}$ is the axial wavenumber, with $n_z \in [-N_z/2, N_z/2-1]$ being an integer and $k_{z0} = 2\pi/L_z$ being the smallest positive wavenumber. The axial wavelength is defined as $\lambda_z = 2\pi/k_z$, non-dimensionalized as $\lambda_z^+ = \lambda_z u_\tau/\nu$.

It is clear from Fig. 6(a) that the mode of the dome peak of $k_z^+\widetilde{Q}_z^+$ (corresponding to the characteristic length scale of the most energetic eddies) is located within $\lambda_z^+ \in [450, 2400]$ in the near-wall region of the non-rotating pipe flow. It results from the hairpin structures of the boundary layer developing over the pipe wall. In response to the axial system rotation, the dome peak reaches its maximum at $Ro_b = 1$ within $\lambda_z^+ \in [610, 2400]$. As Ro_b increases from 1 to 20, the dome peak reduces dramatically, and its mode further moves toward the larger wavelengths. It is known that the axial system rotation induces counterclockwise-rotating secondary-flow structures in the pipe flows known as Taylor columns (at relatively high rotation numbers), which elongate in the axial direction

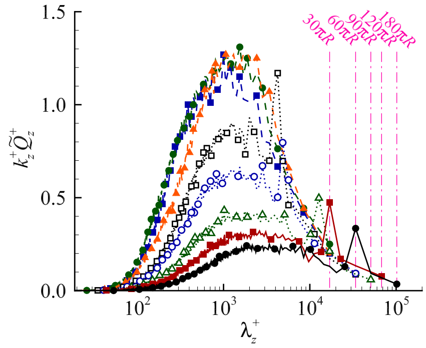

(a) Axial component at $y = 0.093$

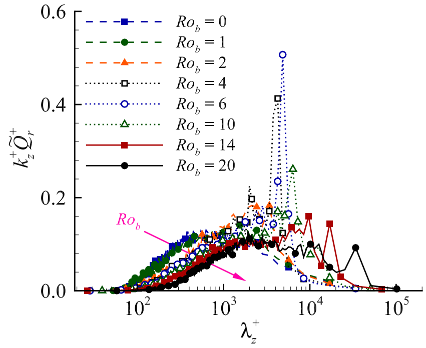

(b) Radial component at $y = 0.187$

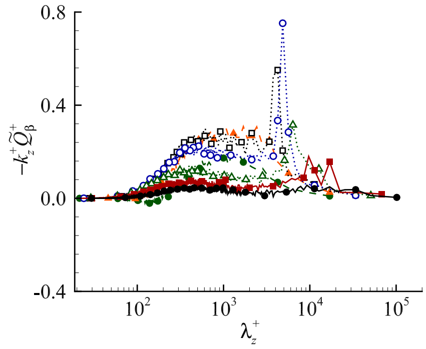

(c) Azimuthal component at $y = 0.058$

Figure 6. Profiles of premultiplied axial cross-spectrum of axial, radial and azimuthal velocity-temperature fluctuations $k_z^+\widetilde{Q}_z^+$, $k_z^+\widetilde{Q}_r^+$ and $k_z^+\widetilde{Q}_\beta^+$ at eight different rotation numbers for $Ro_b = 0$-20, calculated along the streamwise direction at wall-normal position $y = 0.093$, 0.187 and 0.058, respectively.

and spin in the azimuthal direction. Consequently, additional peaks appear at the large wavelengths as Ro_b increases above 4. Clearly, from Fig. 6(a), the axial system rotation tends to weaken the TSE level at high rotation numbers. Similar observations also made in the profiles of $k_z^+\widetilde{Q}_r^+$ and $k_z^+\widetilde{Q}_\beta^+$ shown in Figs. 6(b) and (c), respectively. The additional peaks of $k_z^+\widetilde{Q}_r^+$ and $k_z^+\widetilde{Q}_\beta^+$ occur for $Ro_b \geq 4$. At very high rotation numbers, the magnitudes of $k_z^+\widetilde{Q}_r^+$ and $k_z^+\widetilde{Q}_\beta^+$ become substantially attenuated.

To refine our investigation into the rotating impacts on the turbulent heat fluxes $\langle u_i'\theta'\rangle$, its transport equation can be further studied, viz.

$$\frac{\partial\langle u_i'\theta'\rangle}{\partial t} = C_i + P_i + P_i^t + D_i^t + D_i^p + D_i^m + P_i^c = 0 \quad , \quad (10)$$

where C_i, P_i, P_i^t, D_i^t, D_i^p, D_i^m and P_i^c represent the convection, turbulent production, turbulent production generated from the constant mean axial driving temperature gradient,

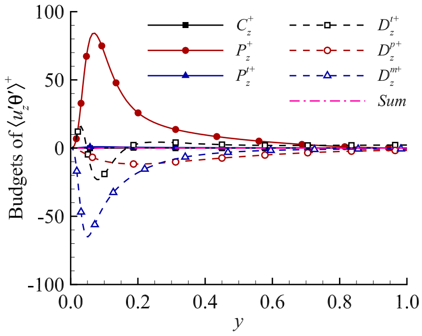

(a) $Ro_b = 0$

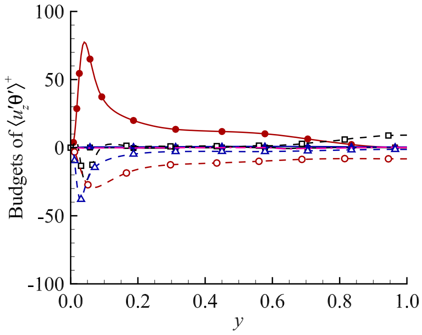

(b) $Ro_b = 20$

Figure 7. Budget balance of axial turbulent heat flux $\langle u_z'\theta'\rangle^+$ of the non-rotating ($Ro_b = 0$) and rotating ($Ro_b = 20$) flows. All budget terms are non-dimensionalized by $u_\tau^2\theta_\tau/R$.

turbulent diffusion, pressure diffusion-redistribution, molecular diffusion-dissipation and Coriolis production terms, respectively. As is shown in Fig. 1, there are only two Coriolis force components in the radial and azimuthal directions. Therefore, only the transport equations of $\langle u_r'\theta'\rangle$ and $\langle u_\beta'\theta'\rangle$ have the Coriolis production terms, i.e., $P_r^c = -2\Omega_z\langle u_\beta'\theta'\rangle$ and $P_\beta^c = 2\Omega_z\langle u_r'\theta'\rangle$.

Figure 7 shows the budget balance of the axial turbulent flux $\langle u_z'\theta'\rangle^+$ of the non-rotating ($Ro_b = 0$) and rotating ($Ro_b = 2$) pipe flows. As is shown in Fig. 7(a), the budget balance of $\langle u_z'\theta'\rangle^+$ is mostly dominated by turbulent production P_z^+ and molecular diffusion-dissipation D_z^{m+} in the near-wall region of the non-rotating pipe flow. More specifically, P_z^+ and D_z^{m+} behave as source and sink terms, respectively. By contrast, at $Ro_b = 20$, the mechanisms of molecular diffusion-dissipation D_z^{m+} and pressure diffusion-redistribution D_z^{p+} are weakened and strengthened, respectively, by the axial system rotation. Consequently, D_z^{m+} and D_z^{p+} become comparable in magnitude and both function as sink terms in the near-wall region of the pipe.

Figure 8 compares the budget balance of the radial turbulent heat flux $\langle u_r'\theta'\rangle^+$ at three different rotation numbers $Ro_b = 0$, 6 and 20. For the non-rotating pipe flow, turbulent production P_r^+ and pressure diffusion-redistribution D_r^{p+} dominate the budget balance of $\langle u_z'\theta'\rangle^+$ in the y-direction, acting as source and sink terms, respectively. However, as Ro_b increases to 6, Coriolis production P_r^{c+} acts as the most dominant source term (surpassing P_r^+) to balance with D_r^{p+}. As Ro_b further increases to 20, it is interesting to observe that the functions of P_r^{c+} and D_r^{p+} are reversed in region $y \in [0.127, 0.578]$. It is interesting to observe that at $Ro_b = 6$ and 20, P_r^{c+} and D_r^{p+} balance each other so well as if they are a mirror reflection of each other. It is clear that the magnitude of D_r^{p+} increases almost ninefold in the near-wall region of the pipe at $Ro_b = 6$ and 20 compared with those of the non-rotating pipe flow in

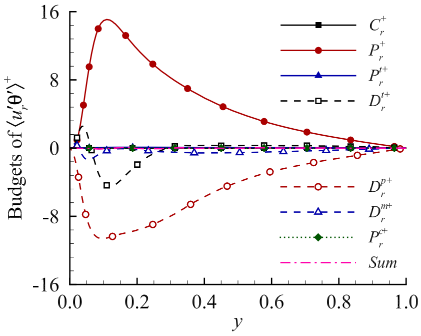

(a) $Ro_b = 0$

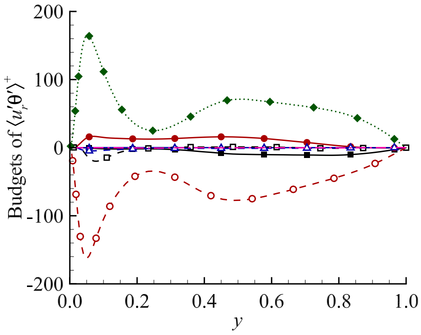

(b) $Ro_b = 6$

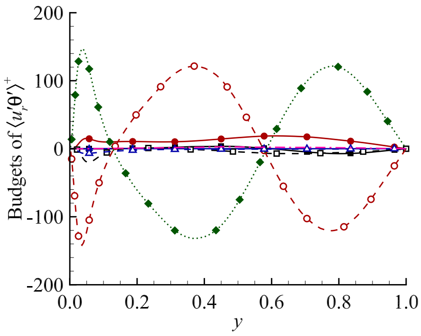

(c) $Ro_b = 20$

Figure 8. Budget balance of radial turbulent heat flux $\langle u_r'\theta'\rangle^+$ of the non-rotating ($Ro_b = 0$) and rotating ($Ro_b = 6$ and 20) flows. All budget terms are non-dimensionalized by $u_\tau^2\theta_\tau/R$.

order to neutralize the significant impact of P_r^{c+}.

Figure 9 compares the budget balance of the azimuthal turbulent heat flux $\langle u_\beta'\theta'\rangle^+$ for two rotating flow cases ($Ro_b =$ 1 and 20). At $Ro_b = 1$, the budget balance of $\langle u_\beta'\theta'\rangle^+$ is mostly dominated by Coriolis production P_β^{c+} and pressure diffusion-redistribution D_β^{p+}. However, at $Ro_b = 20$, the dominance of P_β^{c+} and D_β^{p+} become the most strongly expressed in the transport of $\langle u_\beta'\theta'\rangle^+$. Their magnitudes increase almost fifteenfold in the near-wall region in comparison with those of the rotating pipe flow at $Ro_b = 1$.

Figure 10 compares streaky thermal structures in the β-z plane at $y = 0.127$ for $Ro_b = 0$, 1 and 20, in a domain that is arbitrarily selected with $z/R \in [0, 10]$. At $Ro_b = 0$, the thermal streaks shown by the positively- and negatively-valued θ'^+ alternate in the β-direction. As Ro_b increases to 6, the strengths of those streaks enhance in response to the axial system rotation. However, as Ro_b reaches 20, the positively-valued thermal streaks reduce significantly, while the negatively-valued thermal streaks stretch along the z-direction and tilt slightly along the β-direction, leading to an interruption of the forma-

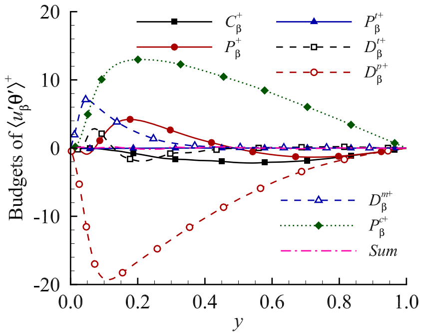

(a) $Ro_b = 1$

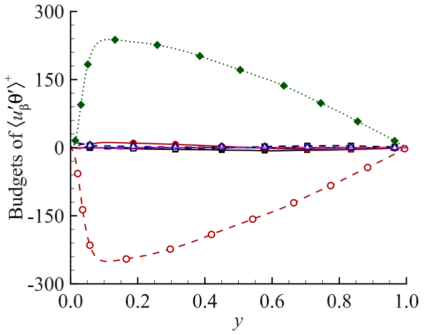

(b) $Ro_b = 20$

Figure 9. Budget balance of azimuthal turbulent heat flux $\langle u'_\beta \theta' \rangle^+$ for two flow cases ($Ro_b = 1$ and 20). All budget terms are non-dimensionalized by $u_\tau^2 \theta_\tau / R$.

tion of hairpin structures.

CONCLUSIONS

Turbulent heat transfer confined within a circular pipe flow subjected to axial rotation has been studied using DNS. In order to thoroughly investigate the Coriolis force impacts on the temperature field, a wide range of rotation numbers varying from $Ro_b = 0$ to 20 have been examined. In response to the axial system rotation, a maximum of $\langle \theta \rangle^+$ is observed at $Ro_b = 1$. As Ro_b further increases, the system rotation tends to reduce $\langle \theta \rangle^+$ in magnitude. Furthermore, the magnitudes of both $\langle \theta' \theta' \rangle^+$ and $\langle u'_z \theta' \rangle^+$ decrease while the Nusselt number increases with an increasing value of Ro_b, indicating that the system rotation functions to suppress the TSE level of the flow.

For the premultiplied turbulent thermal spectra, the dome peak occurs due to the hairpin structures of the boundary layer developing over the pipe wall. The magnitude of the premultiplied cross-spectrum $k_z^+ \widetilde{Q}_z^+$ reaches its maximum at $Ro_b = 1$. As Ro_b continues to increase, its peak value reduces dramatically and its mode moves toward larger wavelengths. It is interesting that additional peaks occur when $Ro_b \geq 4$, which is created by the Taylor columns associated with the axial system rotation imposed.

In the budget balance of turbulent heat fluxes of the axially-rotating pipe flows, the Coriolis force (as indicated by Ω_z) does not directly influence $\langle u'_z \theta' \rangle^+$. For both $\langle u'_r \theta' \rangle^+$ and $\langle u'_z \beta' \rangle^+$, the most dominant terms are the Coriolis production (as a source exceeding turbulent production) and pressure-diffusion redistribution (as a sink). These terms in $\langle u'_r \theta' \rangle^+$ and $\langle u'_\beta \theta' \rangle^+$ balance each other so well as if they are a mirror reflection of each other.

It is interesting to observe that in response to the system rotation imposed, the near-wall thermal streaky structures extend in the z-direction and tilt in the β- direction, resulting in a restriction on the formation of the hairpin structures.

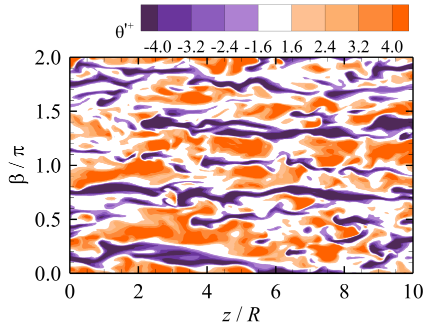

(a) $Ro_b = 0$

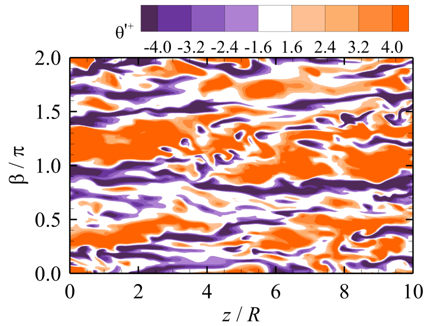

(b) $Ro_b = 1$

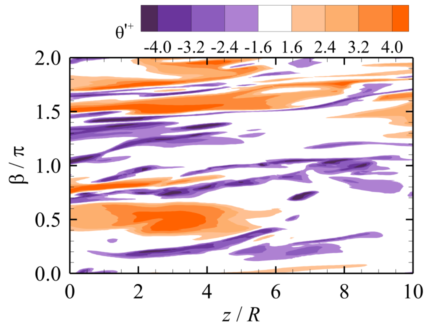

(c) $Ro_b = 20$

Figure 10. Contours of instantaneous temperature fluctuation θ'^+ in the β-z plane at wall normal position $y = 0.127$ for the non-rotating ($Ro_b = 0$) and rotating ($Ro_b = 1$ and 20) flows.

REFERENCES

Blackburn, H. M. & Sherwin, S. J. 2004 Formulation of a Galerkin spectral element-Fourier method for three-dimensional incompressible flows in cylindrical geometries. *J. Comp Phys.* **197** (2), 759–778.

Bousbai, M., Ould-Rouiss, M., Mazouz, A. & Mataoui, A. 2013 Turbulent heat transfer characteristics of water flow in a rotating pipe. *Heat Mass Transf.* **49** (4), 469–484.

Cannon, J. N. & Kays, W. M. 1969 Heat transfer to a fluid flowing inside a pipe rotating about its longitudinal axis. *J. Heat Transf.* **91** (1), 135–139.

Orlandi, P. & Ebstein, D. 2000 Turbulent budgets in rotating pipes by DNS. *Int. J. Heat Fluid Flow* **21**, 499–505.

Ould-Rousis, M., Dries, A. & Mazouz, A. 2010 Numerical predictions of turbulent heat transfer for air flow in rotating pipe. *Int. J. Heat Fluid Flow* **31** (4), 507–517.

Reich, G. & Beer, H. 1989 Fluid flow and heat transfer in an axially rotating pipe - I. Effect of rotation on turbulent pipe flow. *Int. J. Heat Mass Transf.* **32** (3), 551–562.

Satake, S. & Kunugi, T. 2002 Direct numerical simulation of turbulent heat transfer in an axially rotating pipe flow: Reynolds shear stress and scalar flux budgets. *Int. J. Numer. Meth. Heat Fluid Flow* **12** (8), 985–1008.